Geophysical Journal International

Geophys. J. Int. (2014) **196,** 230–242
Advance Access publication 2013 November 15

doi: 10.1093/gji/ggt389

Surface wave retrieval in layered media using seismic interferometry by multidimensional deconvolution

Karel N. van Dalen,[1] Kees Wapenaar[1] and David F. Halliday[2]

[1]*Department of Geoscience and Engineering, Delft University of Technology, Stevinweg* 1, *NL*-2628 *CN Delft, The Netherlands.*
E-mail: k.n.vandalen@tudelft.nl
[2]*Schlumberger Gould Research, High Cross, Madingley Road, Cambridge, CB*3 0*EL, UK*

Accepted 2013 September 23. Received 2013 September 17; in original form 2013 May 3

SUMMARY

Virtual-source surface wave responses can be retrieved using the crosscorrelation (CC) of wavefields observed at two receivers. Higher mode surface waves cannot be properly retrieved when there is a lack of subsurface sources that excite these wavefields, as is often the case. In this paper, we present a multidimensional-deconvolution (MDD) scheme that is based on an approximate convolution theorem. The scheme introduces an additional processing step in which the CC result is deconvolved by a so-called point-spread tensor. The involved point-spread functions capture the imprint of the lack of subsurface sources and possible anelastic effects, and quantify the associated spatial and temporal smearing of the virtual-source components that leads to the poor surface wave retrieval. The functions can be calculated from the same wavefields as used in the CC method. For a 2-D example that is representative of the envisaged applications, we show that the deconvolution partially corrects for the smearing. The retrieved virtual-source response only has some amplitude error in the ideal situation of having the depth of the required vertical array equal to the depth penetration of the surface waves. The error is due to ignored cross-mode terms in the approximate convolution theorem. Shorter arrays are also possible. In the limit case of only a single surface receiver, the retrieved virtual-source response is still more accurate than the CC result. The MDD scheme is valid for horizontally layered media that are laterally invariant, and includes exclusively multicomponent point-force responses (rather than their spatial derivatives) and multicomponent observations. The improved retrieval of multimode surface waves can facilitate dispersion analyses in shallow-subsurface inversion problems and monitoring, and surface wave removal algorithms.

Key words: Interferometry; Surface waves and free oscillations; Interface waves.

1 INTRODUCTION

Seismic interferometry is a technique that uses observations of a wavefield to create virtual seismic sources at locations where only receivers are present. More specifically, by crosscorrelating observations at two different seismic receivers, one retrieves or reconstructs an approximation to the Green's function (i.e. the impulse response or virtual-source response) as if one of the receivers were a source (e.g. Campillo & Paul 2003; Larose *et al.* 2006; Wapenaar & Fokkema 2006; Schuster 2009; Snieder *et al.* 2009). This technique has been used in many different applications. For example, virtual subsurface sources were created using real surface sources (Bakulin & Calvert 2006), and virtual-source reflected waves were retrieved from background noise recordings (Draganov *et al.* 2007); both examples show that body waves can be retrieved successfully.

Surface wave retrieval has received relatively wide attention, which can be explained by the fact that wavefield recordings are often dominated by surface waves, particularly when the sources are located close to the Earth's surface. Applications exist on different scales. In regional seismology, virtual-source surface wave responses can be retrieved by applying interferometry to so-called passive wavefields that are excited by ambient noise sources (such as ocean storms; Shapiro *et al.* 2005) or by earthquakes (by exploiting the seismic coda; Campillo & Paul 2003). Using such ambient noise sources, one can retrieve the virtual-source response at frequencies that are difficult to generate using active sources (Wathelet *et al.* 2004; Park *et al.* 2007). The results are used to determine group velocity images, which is often done based on the fundamental-mode Rayleigh wave only (e.g. Shapiro *et al.* 2005; Gerstoft *et al.* 2006; Bensen *et al.* 2007); in general, the surface wave response in a layered medium consists of a superposition of modes. In exploration seismology, virtual-source surface waves can be retrieved using active sources at the surface. The retrieved surface wave responses are used to guide filters designed to suppress surface waves in seismic data as they overshadow the much weaker body waves reflected at deeper targets of interest (e.g. Halliday *et al.* 2007, 2010). In near-surface seismology and geotechnical engineering, retrieved surface waves, obtained from either active or passive sources, are

used to determine shear wave velocity profiles of the shallow subsurface (Xia *et al.* 1999; Louie 2001; Wathelet *et al.* 2004).

One of the issues for surface wave interferometry has been the source distribution that is required to obtain a reliable interferometry result. Ideally, one needs sources along a contour enclosing the receivers whose observations are crosscorrelated, and the source distribution needs to be regular (Wapenaar & Fokkema 2006). Halliday & Curtis (2008) showed that subsurface sources are required to properly retrieve surface wave responses. In particular, they showed that higher mode surface waves cannot be correctly estimated using their approximate correlation theorem when subsurface sources are absent. Kimman & Trampert (2010) showed that spurious arrivals, coming from non-cancelling cross-mode correlations, might even overwhelm the retrieved higher modes when subsurface sources are absent. The spurious arrivals can be suppressed when there is a homogeneous distribution of sources at the surface, but amplitude and phase errors remain in the retrieved signal (Kimman & Trampert 2010). Another way to improve the interferometric result is to separate the modes in the observed data so that cross-mode correlations are circumvented. In that case, using only surface sources, mainly amplitude errors remain due to missing modal scale factors, but this relies on the ability to identify and separate the various surface wavemodes in the seismic data (e.g. Nolet & Panza 1976).

Nevertheless, the correct retrieval of higher mode surface waves can be beneficial for obtaining information about the subsurface. In particular, the higher mode surface waves provide information about greater depth ranges than the fundamental mode, and their presence enhances the depth resolution of the near-surface velocity models when joint inversion of the fundamental and higher modes is applied (MacBeth & Burton 1985; Dost 1990; Beaty *et al.* 2002; Xia *et al.* 2003). The retrieval of the higher modes could be improved by using a recently developed modification to the seismic-interferometry technique called 'seismic interferometry by multidimensional deconvolution (MDD)' (Wapenaar *et al.* 2011b). In heuristic terms, the modification consists of an additional processing step where the crosscorrelation (CC) result is deconvolved by the so-called point-spread function. This point-spread function captures the lack of equipartitioning of the sources (and the possible anelastic effects) and quantifies the associated smearing of the virtual source in space and time; the more smearing, the worse the correlation result. Deconvolving by the point-spread function can partially correct for the smearing of the virtual source. The virtual source then becomes more ideal in space and time, and the retrieved virtual-source response is expected to become more accurate. The point-spread function can be calculated from the same wavefields used in the correlation method. MDD has been shown to improve the retrieval of the fundamental-mode surface wave for non-ideal surface-source distribution (Wapenaar *et al.* 2011a), but has not yet been applied to improve the retrieval of higher mode surface waves.

In this paper, we apply MDD to retrieve the full surface wave response (including the higher modes). We propose an MDD scheme that is particularly suited for surface waves in horizontally layered media. It is based on an approximate convolution theorem that contains exclusively point-force responses rather than their spatial derivatives, which is advantageous in view of potential field applications. The performance of the MDD scheme is illustrated using numerical examples. Results show that the virtual-source response, including the higher mode surface waves, can be retrieved accurately, especially compared to the results of the CC method.

In Section 2, we evaluate the integral in the convolution-type reciprocity theorem using a stationary-phase analysis. We use this analysis to determine the modal scale factors of the proposed approximate convolution theorem in Section 3. In Section 4, we derive the MDD scheme; numerical examples are shown in Section 5. The envisaged applications of the MDD scheme in a geophysical context are discussed in Section 6. Finally, we summarize our conclusions in Section 7.

2 STATIONARY-PHASE ANALYSIS OF CONVOLUTION THEOREM

In this section, we apply the convolution-type reciprocity theorem to surface wave responses and evaluate the associated integral using the stationary-phase method. Snieder (2004) and Halliday & Curtis (2008) did a similar derivation for the correlation-type reciprocity theorem. In the next section, we use the results to derive an approximate convolution theorem for surface waves.

Throughout this paper, we adopt the following Fourier transform over time for an arbitrary function $f(\mathbf{x}, t)$:

$$\hat{f}(\mathbf{x}, \omega) = \int_{-\infty}^{\infty} f(\mathbf{x}, t) \exp(-\mathrm{i}\omega t)\, \mathrm{d}t, \tag{1}$$

where ω denotes angular frequency, t denotes time and $\mathbf{x} = [x, y, z]^T$ is a vector containing spatial coordinates. The hat refers to the $(\mathbf{x}, \omega)$ domain. From here onwards, the ω dependence is left out for brevity [i.e. $\hat{f}(\mathbf{x}) = \hat{f}(\mathbf{x}, \omega)$]. All considered functions are real-valued in the space–time domain, and it is therefore sufficient to consider $\omega \geq 0$.

The space–frequency domain elastodynamic convolution-type reciprocity theorem reads (de Hoop 1995; Aki & Richards 2002)

$$\hat{G}_{im}(\mathbf{x}_R, \mathbf{x}_S) = \int_S \Big[\hat{G}_{in}(\mathbf{x}_R, \mathbf{x}) n_j c_{njkl}(\mathbf{x}) \partial_k \hat{G}_{lm}(\mathbf{x}, \mathbf{x}_S) - n_j c_{njkl}(\mathbf{x}) \partial_k \hat{G}_{il}(\mathbf{x}_R, \mathbf{x}) \hat{G}_{nm}(\mathbf{x}, \mathbf{x}_S) \Big]\, \mathrm{d}S, \tag{2}$$

where S denotes the enclosing boundary of a volume V, which has outward-pointing unit normal n_j (see Fig. 1, where we consider the specific case of a cylindrical volume in view of the analysis below); summation is invoked over repeated indices, but not over the Greek indices introduced below. The integral in the convolution theorem describes forward propagation of a wavefield, which is excited at $\mathbf{x}_S$ (located outside V), from observations at $\mathbf{x}$ (located at S) to receiver $\mathbf{x}_R$ (located inside V). In fact, the receivers along S act as secondary sources that forward propagate the wavefield to $\mathbf{x}_R$. The Green's tensors (e.g. $\hat{G}_{im}$) in eq. (2) are force-source Green's tensors for particle displacement and c_{njkl} denotes the elasticity tensor. The partial derivative operators act on $\mathbf{x}$.

In this paper, we only consider the surface wave part of the Green's tensors. This could be valid in places where the surface wave is the dominant wave type. For horizontally layered media with a free surface and a half-space below the layering, the force-source surface wave Green's tensors can be represented in the far field by a sum over modes (Aki & Richards 2002; Snieder 2002):

$$\hat{G}_{nm}(\mathbf{x}, \mathbf{x}_S) = \textstyle\sum_\nu p_n^\nu(z, \varphi_S) p_m^{\nu *}(z_S, \varphi_S) \dfrac{\mathrm{e}^{-\mathrm{i}\left(k_\nu \xi_S + \frac{\pi}{4}\right)}}{\chi_\nu \sqrt{\frac{\pi}{2} k_\nu \xi_S}}, \tag{3}$$

where the * denotes complex conjugation and the ν indicates a specific mode; $\hat{G}_{in}(\mathbf{x}_R, \mathbf{x})$ has a very similar expression. The horizontal offsets are given by

$$\xi_S = \sqrt{(x - x_S)^2 + (y - y_S)^2}, \tag{4}$$

$$\xi_R = \sqrt{(x_R - x)^2 + (y_R - y)^2}. \tag{5}$$

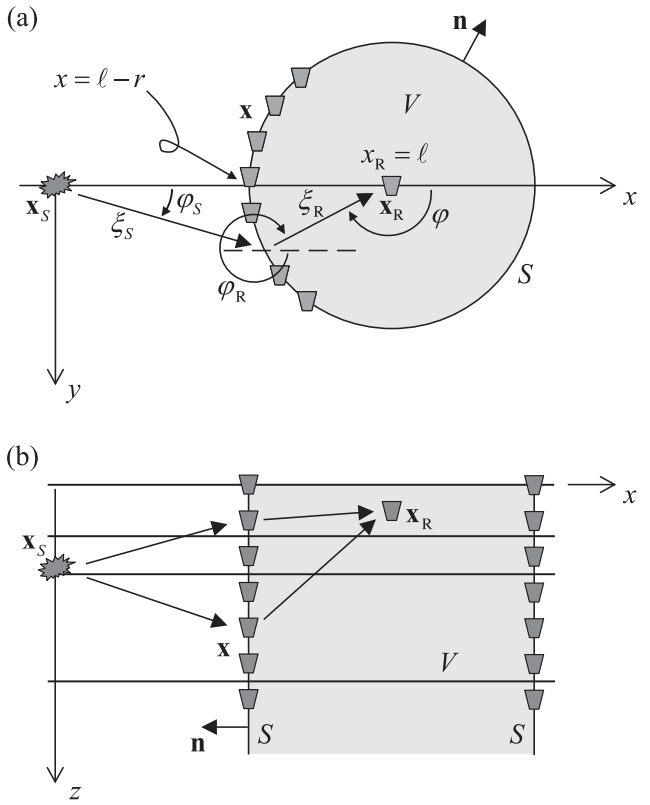

Figure 1. Plan view (a) and cross-section (b) of cylindrical volume V enclosed by surface S, having outward-pointing unit normal $\mathbf{n}$, used for forward propagation of a wavefield from $\mathbf{x}_S$ via $\mathbf{x}$ to $\mathbf{x}_R$. The medium is horizontally layered and laterally (x, y plane) invariant.

Furthermore, z_S and z_R are the depth coordinates associated with $\mathbf{x}_S$ and $\mathbf{x}_R$, respectively, φ_S and φ_R are angles in the horizontal plane that indicate the directions from $\mathbf{x}_S$ to $\mathbf{x}$ and from $\mathbf{x}$ to $\mathbf{x}_R$ (see Fig. 1) and z is the depth coordinate that belongs to $\mathbf{x}$. The $p_m^{\nu}(z_S, \varphi_S)$ and $p_n^{\nu}(z, \varphi_S)$ are components of polarization vectors at $\mathbf{x}_S$ and $\mathbf{x}$, respectively, k_ν is the wavenumber of surface wavemode and χ_ν is a factor depending on the phase velocity, the group velocity and the modal kinetic energy (see Appendix A). The tensors in eq. (2) that include the partial derivative operator at $\mathbf{x}$ represent the traction due to a force source or the particle motion due to a deformation-rate source, respectively, depending on whether $\mathbf{x}$ represents a receiver or a source.

Substituting the appropriate Green's tensors into the convolution theorem, we obtain

$$\hat{G}_{im}(\mathbf{x}_R, \mathbf{x}_S) = \sum_{\bar{\nu}} \sum_{\nu} \int_S p_i^{\nu}(z_R, \varphi_R) p_m^{\bar{\nu}*}(z_S, \varphi_S) \times Q^{\nu,\bar{\nu}}(z, \varphi_R, \varphi_S) \frac{\mathrm{e}^{-\mathrm{i}\left(k_\nu \xi_R + k_{\bar{\nu}} \xi_S + \frac{\pi}{2}\right)}}{\frac{\pi}{2} \chi_\nu \chi_{\bar{\nu}} \sqrt{k_\nu k_{\bar{\nu}} \xi_R \xi_S}} \,\mathrm{d}S, \tag{6}$$

where

$$Q^{\nu,\bar{\nu}} = p_n^{\nu*}(z, \varphi_R) T_n^{\bar{\nu}}(z, \varphi_S) - T_n^{\nu*}(z, \varphi_R) p_n^{\bar{\nu}}(z, \varphi_S), \tag{7}$$

and where T_n^{ν} represents a traction vector at $\mathbf{x}$, which has been obtained using the expression of the stiffness tensor c_{njkl} for isotropic media (see Appendix A).

We consider the specific configuration of a cylindrical volume V with radius r, as displayed in Fig. 1. For convenience, $\mathbf{x}_S$ and $\mathbf{x}_R$ are chosen in the x, z plane with $x_S = 0$ and $x_R = \ell$ (centre of the cylinder), respectively; the analysis below is, however, generally valid. In addition, we take the limit case of an infinitely long cylinder so that the integrand of eq. (6) vanishes at the bottom part of S due to the decay of the surface waves in vertical direction. As the top part of S lies at the free surface, across which the normal and shear stresses are zero and hence $Q^{\nu,\bar{\nu}} = 0$, only the integration over the vertical part of S remains. Using cylindrical coordinates ($\mathrm{d}S = r\mathrm{d}\varphi\mathrm{d}z$), the integral in eq. (6), which we denote as $\Lambda_{im}^{\nu,\bar{\nu}}$, can be written as

$$\Lambda_{im}^{\nu,\bar{\nu}} = \mathrm{e}^{-\mathrm{i}\frac{\pi}{2}} \int_0^{\infty} \Phi_{im}^{\nu,\bar{\nu}} \,\mathrm{d}z, \tag{8}$$

where

$$\Phi_{im}^{\nu,\bar{\nu}} = \int_0^{2\pi} \mathrm{e}^{-\mathrm{i}k_\nu r \psi(\varphi)} F_{im}^{\nu,\bar{\nu}}(z, z_R, z_S, \varphi_R, \varphi_S) r \,\mathrm{d}\varphi, \tag{9}$$

with

$$F_{im}^{\nu,\bar{\nu}} = p_i^{\nu}(z_R, \varphi_R) p_m^{\bar{\nu}*}(z_S, \varphi_S) \frac{Q^{\nu,\bar{\nu}}(z, \varphi_R, \varphi_S)}{\frac{\pi}{2} \chi_\nu \chi_{\bar{\nu}} \sqrt{k_\nu k_{\bar{\nu}} r \xi_S}}. \tag{10}$$

Here, we used that $\xi_R = r$ (see Fig. 1a), and

$$\psi(\varphi) = 1 + \frac{k_{\bar{\nu}} \xi_S}{k_\nu r}. \tag{11}$$

We evaluate the integral over φ in eq. (9) using the stationary-phase method (Jeffreys & Jeffreys 1946; Achenbach 1973), which assumes that $k_\nu r$ is large (far-field assumption) and $F_{im}^{\nu,\bar{\nu}}$ varies relatively slowly with φ (note that φ_S and φ_R vary with φ); $k_{\bar{\nu}} \xi_S$ is assumed large as well. Using eqs (4) and (5), and $x = \ell + r\cos(\varphi)$ and $y = r\sin(\varphi)$, we can show that the phase of the exponential factor in eq. (9) is stationary at $\varphi = \varphi_1 = \pi$ and at $\varphi = \varphi_2 = 0$ (i.e. $\partial\psi/\partial\varphi = 0$). At the first stationary point, $\varphi_S^{(1)} = 0$, $\varphi_R^{(1)} = 2\pi$ and $\xi_S^{(1)} = \ell - r$ so that $\mathbf{x}_S$, $\mathbf{x}$ and $\mathbf{x}_R$ lie in the same vertical plane (the x, z plane; see Fig. 1). At the second stationary point, $\mathbf{x}_S$, $\mathbf{x}$ and $\mathbf{x}_R$ also lie in the x, z plane and $\varphi_S^{(2)} = 0$, but $\varphi_R^{(2)} = \pi$ and $\xi_S^{(2)} = \ell + r$ (the second stationary point lies at the opposite side of S, compared to the first). The integration over φ can now be approximated as (Achenbach 1973)

$$\Phi_{im}^{\nu,\bar{\nu}} \cong \sum_{j=1}^{2} \sqrt{\frac{2\pi}{k_\nu r |\psi''(\varphi_j)|}} \mathrm{e}^{-\mathrm{i}k_\nu r \psi(\varphi_j) \mp \mathrm{i}\frac{\pi}{4}} \times F_{im}^{\nu,\bar{\nu}}\left[z, z_R, z_S, \varphi_R^{(j)}, \varphi_S^{(j)}\right] r, \tag{12}$$

where $\psi''(\varphi_j) = \partial^2\psi/\partial\varphi^2|_{\varphi=\varphi_j}$, and the upper and lower signs relate to $\psi''(\varphi_j) > 0$ and $\psi''(\varphi_j) < 0$, respectively. Using

$$\psi(\varphi_j) = 1 + \frac{k_{\bar{\nu}}}{k_\nu} \frac{\ell \mp r}{r}, \quad \psi''(\varphi_j) = \pm \frac{k_{\bar{\nu}}}{k_\nu} \frac{\ell}{\ell \mp r}, \tag{13}$$

eq. (12) can be written as

$$\Phi_{im}^{\nu,\bar{\nu}} \cong \sum_{j=1}^{2} p_i^{\nu}\left[z_R, \varphi_R^{(j)}\right] p_m^{\bar{\nu}*}\left[z_S, \varphi_S^{(j)}\right] Q^{\nu,\bar{\nu}}\left[z, \varphi_R^{(j)}, \varphi_S^{(j)}\right] \times \frac{1}{\chi_\nu \chi_{\bar{\nu}}} \sqrt{\frac{8}{\pi k_\nu k_{\bar{\nu}}^2 \ell}} \mathrm{e}^{-\mathrm{i}\left[k_\nu r + k_{\bar{\nu}}(\ell \mp r) \pm \frac{\pi}{4}\right]}, \tag{14}$$

where the upper and lower signs relate to the $j = 1$ and $j = 2$, respectively. Next, we compute the integral over depth z. This reduces to the integral of $Q^{\nu,\bar{\nu}}[z, \varphi_R^{(j)}, \varphi_S^{(j)}]$ only (*cf.* eqs 7–10). We separate between the cases $\nu \neq \bar{\nu}$ (cross-mode contributions) and $\nu = \bar{\nu}$ (principal contributions). Using the orthogonality relation for Rayleigh waves (Aki & Richards 2002), we find that

$$\int_0^{\infty} Q^{\nu,\bar{\nu}}\left[z, \varphi_R^{(j)}, \varphi_S^{(j)}\right] \mathrm{d}z = 0, \quad \nu \neq \bar{\nu}. \tag{15}$$

The cross-mode contributions thus vanish. Furthermore, it appears that $Q^{\nu,\nu}[z,\varphi_R^{(2)},\varphi_S^{(2)}]=0$. Therefore, the second stationary point does not contribute to the integral in eq. (6), which is reasonable as there is no wave travelling from $\mathbf{x}_S$ to $\mathbf{x}_R$ via $\mathbf{x}$ when the latter lies at the rightmost side of S (see Fig. 1). For the principal contributions at the first stationary point, we find (*cf.* Halliday & Curtis 2008)

$$\int_0^\infty Q^{\nu,\nu}\left[z,\varphi_R^{(1)},\varphi_S^{(1)}\right]\,\mathrm{d}z = 4\mathrm{i}k_\nu\Delta_1 c_\nu U_\nu I_1^\nu, \tag{16}$$

where c_ν, U_ν and I_1^ν are the phase velocity, the group velocity and the kinetic energy of mode ν (see Appendix A), respectively, and

$$\Delta_1 = \cos(\varphi_1)n_x^{(1)} + \sin(\varphi_1)n_y^{(1)} = 1. \tag{17}$$

Here, $n_x^{(1)}$ and $n_y^{(1)}$ are the horizontal components of the outward-pointing unit normal of S at the stationary point (*cf.* Fig. 1): $n_x^{(1)}=-1$ and $n_y^{(1)}=0$. In general, $n_x^{(1)}=\cos(\varphi_1)$, $n_y^{(1)}=\sin(\varphi_1)$ and $n_z^{(1)}=0$. We note that z_S and z_R can be different; $n_z^{(1)}=0$ as the normal is always oriented in the horizontal plane. Taking the results together according to eq. (8) and using eq. (A3), we find

$$\Lambda_{im}^{\nu,\nu} \cong p_i^\nu\left[z_R,\varphi_R^{(1)}\right]p_m^{\nu*}\left[z_S,\varphi_S^{(1)}\right]\frac{\mathrm{e}^{-\mathrm{i}\left(k_\nu\ell+\frac{\pi}{4}\right)}}{\chi_\nu\sqrt{\frac{\pi}{2}k_\nu\ell}}. \tag{18}$$

Now, using the replacements $\ell\rightarrow\xi_{RS}$ and $\varphi_S^{(1)}=\varphi_R^{(1)}\rightarrow\varphi_{RS}$, where the subscript RS indicates that ξ and φ belong to the straight line from $\mathbf{x}_S$ to $\mathbf{x}_R$, we obtain (from eqs 6, 8 and 18)

$$\hat{G}_{im}(\mathbf{x}_R,\mathbf{x}_S) \cong \sum_\nu p_i^\nu(z_R,\varphi_{RS})p_m^{\nu*}(z_S,\varphi_{RS})\frac{\mathrm{e}^{-\mathrm{i}\left(k_\nu\xi_{RS}+\frac{\pi}{4}\right)}}{\chi_\nu\sqrt{\frac{\pi}{2}k_\nu\xi_{RS}}}, \tag{19}$$

which is the point-force response (*cf.* eq. 3); in the current stationary-phase analysis, the point-force response is obtained approximately, because the integral over φ has not been evaluated exactly (*cf.* eq. 14).

In the next section, we use one of the steps of the above analysis, particularly the integration over depth (see eq. 16), to derive an approximate convolution theorem which yields the same Green's function in the stationary-phase analysis.

3 APPROXIMATE CONVOLUTION THEOREM

Halliday & Curtis (2008) derived an approximate correlation theorem that contains exclusively point-force surface wave Green's functions. It can be written as (Kimman & Trampert 2010)

$$\hat{G}_{im}^\nu(\mathbf{x}_A,\mathbf{x}_B) - \hat{G}_{im}^{\nu*}(\mathbf{x}_A,\mathbf{x}_B)$$
$$\cong -\int_S \mathrm{i}\omega\hat{A}_\nu\hat{G}_{in}^\nu(\mathbf{x}_A,\mathbf{x})\hat{G}_{mn}^{\nu*}(\mathbf{x}_B,\mathbf{x})\,\mathrm{d}S, \tag{20}$$

where $\mathbf{x}_A$ and $\mathbf{x}_B$ are receivers both located inside a volume that has sources $\mathbf{x}$ all over its enclosing boundary S. The approximate correlation theorem contains modal scale factors $\hat{A}_\nu=\hat{A}_\nu(\omega)$ that have been determined so that the integral in the right-hand side gives the same result as that in the original correlation theorem in the stationary-phase analysis (see Halliday & Curtis 2008). Eq. (20) holds for each mode separately; if one inserts the entire responses in the right-hand side (without modal separation), cross-mode contributions are introduced.

Here, we propose an approximate convolution theorem that is very similar to the approximate correlation theorem

$$\hat{G}_{im}^\nu(\mathbf{x}_R,\mathbf{x}_S) \cong \int_S -\mathrm{i}k_\nu\hat{B}_\nu\hat{G}_{in}^\nu(\mathbf{x}_R,\mathbf{x})\hat{G}_{nm}^\nu(\mathbf{x},\mathbf{x}_S)\,\mathrm{d}S, \tag{21}$$

where the $\hat{B}_\nu$ are modal scale factors to compensate for the absence of the spatial derivatives (*cf.* eq. 2). When all modes are considered together, the theorem can be written as

$$\hat{G}_{im}(\mathbf{x}_R,\mathbf{x}_S) + \hat{G}_{im}^c(\mathbf{x}_R,\mathbf{x}_S) \cong \int_S \hat{W}_{in}(\mathbf{x}_R,\mathbf{x})\hat{G}_{nm}(\mathbf{x},\mathbf{x}_S)\,\mathrm{d}S, \tag{22}$$

where $\hat{G}_{im}^c(\mathbf{x}_R,\mathbf{x}_S)$ denotes the contribution of the introduced cross terms, and

$$\hat{W}_{in}(\mathbf{x}_R,\mathbf{x}) = \sum_\nu -\mathrm{i}k_\nu\hat{B}_\nu\hat{G}_{in}^\nu(\mathbf{x}_R,\mathbf{x})$$
$$= \sum_\nu -\mathrm{i}k_\nu\hat{B}_\nu p_i^\nu(z_R,\varphi_R)p_n^{\nu*}(z,\varphi_R)\frac{\mathrm{e}^{-\mathrm{i}\left(k_\nu\xi_R+\frac{\pi}{4}\right)}}{\chi_\nu\sqrt{\frac{\pi}{2}k_\nu\xi_R}}. \tag{23}$$

Here, $\hat{W}_{in}(\mathbf{x}_R,\mathbf{x})$ can be thought of as an approximate propagator that brings the wavefield from $\mathbf{x}$ to $\mathbf{x}_R$; it can be considered as a weighted dipole response as it can be obtained by applying a normal derivative $n_j\partial_j$ (at the source coordinate) to the point-force Green's tensor (*cf.* Wapenaar *et al.* 2011b), and multiplying by the factors $\hat{B}_\nu$. In this specific case, n_j is the outward-pointing unit normal vector of a vertical plane, and only the far-field term of the derivative should be included.

To determine the modal scale factors, we perform the same stationary-phase analysis as in Section 2, but now starting from the approximate convolution theorem eq. (22). Substituting the appropriate Green's tensors (eqs 3 and 23), we obtain

$$\hat{G}_{im}(\mathbf{x}_R,\mathbf{x}_S) + \hat{G}_{im}^c(\mathbf{x}_R,\mathbf{x}_S) \cong \sum_{\bar\nu}\sum_\nu\int_S p_i^\nu(z_R,\varphi_R)$$
$$\times\, p_m^{\bar\nu*}(z_S,\varphi_S)R^{\nu,\bar\nu}(z,\varphi_R,\varphi_S)\frac{\mathrm{e}^{-\mathrm{i}\left(k_\nu\xi_R+k_{\bar\nu}\xi_S+\frac{\pi}{2}\right)}}{\frac{\pi}{2}\chi_\nu\chi_{\bar\nu}\sqrt{k_\nu k_{\bar\nu}\xi_R\xi_S}}\,\mathrm{d}S, \tag{24}$$

where

$$R^{\nu,\bar\nu} = -\mathrm{i}k_\nu\hat{B}_\nu p_n^{\nu*}(z,\varphi_R)p_n^{\bar\nu}(z,\varphi_S). \tag{25}$$

For the cylindrical volume V displayed in Fig. 1, the integral in eq. (24) can be written in the same way as in eqs (8)–(10); the only difference lies in the expressions of $Q^{\nu,\bar\nu}(z,\varphi_R,\varphi_S)$ and $R^{\nu,\bar\nu}(z,\varphi_R,\varphi_S)$. Hence, the integration over φ gives a very similar expression as in eq. (14). For the depth integration at the first stationary point, we find

$$\int_0^\infty R^{\nu,\bar\nu}\left[z,\varphi_R^{(1)},\varphi_S^{(1)}\right]\,\mathrm{d}z = -2\mathrm{i}k_\nu\hat{B}_\nu J_1^{\nu,\bar\nu}, \tag{26}$$

where

$$J_1^{\nu,\bar\nu} = \frac{1}{2}\int_0^\infty\left(r_1^\nu r_1^{\bar\nu} + r_2^\nu r_2^{\bar\nu}\right)\,\mathrm{d}z. \tag{27}$$

This integral is similar to that of the modal kinetic energy I_1^ν (Appendix A). For the principal terms ($\nu=\bar\nu$), we now choose the modal scale factors so that the depth integration gives the same result as that in the analysis associated with the original convolution theorem. Comparing eqs (16) and (26), we find

$$\hat{B}_\nu = -2c_\nu U_\nu\frac{I_1^\nu}{J_1^{\nu,\nu}}. \tag{28}$$

Furthermore, we find that $R^{\nu,\nu}[z,\varphi_R^{(2)},\varphi_S^{(2)}]\neq 0$. Hence, the second stationary point now does have a contribution in the integral in eq. (24); this is different in the analysis of the original convolution theorem, where the contribution at the second stationary point in fact vanished on account of Sommerfeld's radiation condition.

For consistency, we therefore replace $\hat{G}_{nm}(\mathbf{x}, \mathbf{x}_S)$ in eq. (22) by the inward-propagating wavefield $\hat{G}^{\text{in}}_{nm}(\mathbf{x}, \mathbf{x}_S)$ so that the integrand automatically vanishes at the second stationary point.

The cross-mode contributions ($\nu \neq \bar{\nu}$) do not vanish in eq. (26), as the orthogonality of the modes is not fulfilled due to the approximation in the convolution theorem. Using eq. (24) and leaving out the contribution of the second stationary point (consistent with above-described choice), we can verify that that their contribution reads

$$\hat{G}^{c}_{im}(\mathbf{x}_R, \mathbf{x}_S) \cong -4 \sum_{\bar{\nu}\neq\nu} \sum_{\nu} p_i^{\nu} \left[z_R, \varphi_R^{(1)}\right] p_m^{\bar{\nu}*} \left[z_S, \varphi_S^{(1)}\right] \times \hat{B}_{\nu} J_1^{\nu,\bar{\nu}} \frac{\mathrm{e}^{-\mathrm{i}\left[k_{\nu} r + k_{\bar{\nu}}(\ell - r) + \frac{\pi}{4}\right]}}{\chi_{\nu}\chi_{\bar{\nu}}\sqrt{\frac{\pi}{2} k_{\bar{\nu}}^2 \ell / k_{\nu}}}. \tag{29}$$

Taking all results together, the approximate convolution theorem thus reads

$$\hat{G}_{im}(\mathbf{x}_R, \mathbf{x}_S) + \hat{G}^{c}_{im}(\mathbf{x}_R, \mathbf{x}_S) \cong \int_S \hat{W}_{in}(\mathbf{x}_R, \mathbf{x}) \hat{G}^{\text{in}}_{nm}(\mathbf{x}, \mathbf{x}_S)\, \mathrm{d}S, \tag{30}$$

where $\hat{W}_{in}(\mathbf{x}_R, \mathbf{x})$ is defined in eq. (23), the modal scale factors $\hat{B}_{\nu}$ in eq. (28) and the cross terms $\hat{G}^{c}_{im}(\mathbf{x}_R, \mathbf{x}_S)$ in eq. (29). Eq. (30) can be used to approximate forward wave propagation of surface waves in horizontally layered media when only point-force Green's functions are present, but the cross terms cannot be avoided. From their phase, we observe that they might interfere with the principal terms of the surface wave tensor, which could be problematic depending on their strength. It is probably impossible to predict the magnitude of the cross terms for arbitrary layering. Therefore, we only assess this issue numerically in the next section.

4 MDD SCHEME

In this section, we derive an MDD scheme that is particularly suited for surface waves in horizontally layered media that are laterally invariant. We take the approximate convolution theorem as the starting point rather than the original one, because the former includes exclusively point-force Green's functions. This is advantageous for applications with contemporary field-acquisition geometries.

The general configuration for the MDD scheme is displayed in Fig. 2. The configuration is similar to that in Fig. 1, but now more sources $\mathbf{x}_S^{(j)}$ are present outside V. We also incorporated several receivers $\mathbf{x}_R$ to create a virtual-shot record (see Section 5). First, we consider the approximate convolution theorem for each of the sources [eq. 30 with $\mathbf{x}_S \rightarrow \mathbf{x}_S^{(j)}$]. By introducing a new coordinate $\mathbf{x}'$ (to distinguish it from the integration coordinate $\mathbf{x}$), we correlate both the left- and right-hand sides with the inward-propagating field at S and sum over source components. Taking the equations of all sources together, we obtain

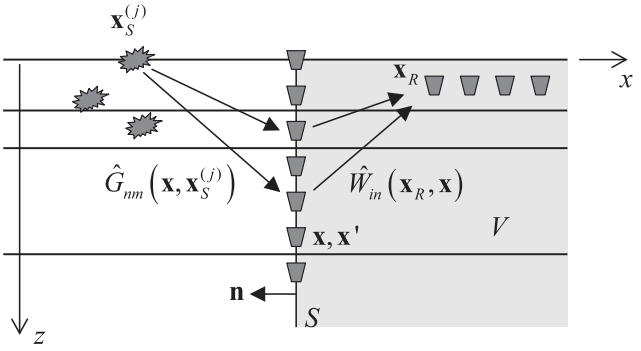

Figure 2. General configuration for the multidimensional deconvolution scheme derived in Section 4. Several sources are present outside volume V. Its enclosing boundary S (having outward-pointing unit normal $\mathbf{n}$) is covered with receivers $\mathbf{x}$; $\mathbf{x}'$ is an auxiliary coordinate.

$$\hat{C}_{ik}(\mathbf{x}_R, \mathbf{x}') \cong \int_S \hat{W}_{in}(\mathbf{x}_R, \mathbf{x}) \hat{\Gamma}_{nk}(\mathbf{x}, \mathbf{x}')\, \mathrm{d}S, \tag{31}$$

where

$$\hat{C}_{ik}(\mathbf{x}_R, \mathbf{x}') = \sum_j \hat{G}_{im}\left(\mathbf{x}_R, \mathbf{x}_S^{(j)}\right) \hat{G}^{\text{in}*}_{km}\left(\mathbf{x}', \mathbf{x}_S^{(j)}\right) \hat{P}^{(j,m)}, \tag{32}$$

$$\hat{\Gamma}_{nk}(\mathbf{x}, \mathbf{x}') = \sum_j \hat{G}^{\text{in}}_{nm}\left(\mathbf{x}, \mathbf{x}_S^{(j)}\right) \hat{G}^{\text{in}*}_{km}\left(\mathbf{x}', \mathbf{x}_S^{(j)}\right) \hat{P}^{(j,m)}. \tag{33}$$

Here, $\hat{P}^{(j,m)} = \hat{P}^{(j,m)}(\omega)$ is the power spectrum of component m of source j.

Following Wapenaar *et al.* (2011b), we address the $\hat{C}_{ik}(\mathbf{x}_R, \mathbf{x}')$ as the correlation tensor and the $\hat{\Gamma}_{nk}(\mathbf{x}, \mathbf{x}')$ as the point-spread tensor (Wapenaar *et al.* 2011b). The involved correlation functions (individual components) can be used to estimate the virtual-source responses, but the result is not ideal (Halliday & Curtis 2008; Kimman & Trampert 2010); we refer to this as the CC method. According to eq. (31), each of the correlation functions can be expressed as a generalized convolution over space and time of propagators and associated point-spread functions, where the latter can be interpreted as virtual-source components. A poor CC result can therefore be explicitly linked to smeared point-spread functions: the more this smearing, the poorer the obtained virtual-source response (Wapenaar *et al.* 2011b). Halliday & Curtis (2008) and Kimman & Trampert (2010) showed that especially higher mode surface waves are poorly retrieved using the CC method when there is a lack of physical subsurface sources. In terms of the current analysis, this implies relatively strong smearing of the point-spread functions. The MDD process, used to calculate the $\hat{W}_{in}(\mathbf{x}_R, \mathbf{x})$ from the correlation and point-spread tensors (eq. 31), can correct for this smearing so that the virtual-source components become more ideal in space and time (Wapenaar *et al.* 2011b); the retrieved higher mode surface waves are then expected to become more accurate.

Both the correlation and point-spread tensors can be calculated directly from the wavefield observations, provided that all required receivers are present: along surface S and one (or more) inside V. To calculate the $\hat{W}_{in}(\mathbf{x}_R, \mathbf{x})$, we discretize eq. (31). In addition, we need to consider different combinations of i and k. Otherwise, we only have more unknowns than equations. We restrict the discussion here to the 2-D case in view of the envisaged applications (see Sections 5 and 6), but an extension to the 3-D case is straightforward. When multicomponent sources and observations are present, the following system of four matrix equations and four unknown submatrices is obtained:

$$\hat{\mathbf{C}} \cong \hat{\mathbf{W}} \hat{\mathbf{\Gamma}}, \tag{34}$$

where the correlation matrix is organized as

$$\hat{\mathbf{C}} = \begin{bmatrix} \hat{\mathbf{C}}_{xx} & \hat{\mathbf{C}}_{xz} \\ \hat{\mathbf{C}}_{zx} & \hat{\mathbf{C}}_{zz} \end{bmatrix}, \tag{35}$$

and the propagator matrix $\hat{\mathbf{W}}$ and the point-spread matrix $\hat{\mathbf{\Gamma}}$ are organized similarly; the matrices are discretized versions of the corresponding tensors. In eq. (35), the $\mathbf{C}_{ik}$ are submatrices with rows and columns corresponding to discrete $\mathbf{x}_R$ and $\mathbf{x}'$, respectively (Wapenaar & Berkhout 1989). Now, $\hat{\mathbf{W}}$ can be obtained

approximately by matrix inversion of $\hat{\mathbf{\Gamma}}$, which should be performed in a stabilized way (see also Section 5). Hence, we get

$$\hat{\mathbf{W}}\hat{\mathbf{\Upsilon}} \cong \hat{\mathbf{C}}\hat{\mathbf{\Gamma}}^{-1}, \tag{36}$$

where $\hat{\mathbf{\Upsilon}} = \hat{\mathbf{\Gamma}}\hat{\mathbf{\Gamma}}^{-1}$; this matrix product does not exactly yield the identity matrix as $\hat{\mathbf{\Gamma}}^{-1}$ is a stabilized inverse. Eq. (36) thus describes a discretized deconvolution; the deconvolution is referred to as multidimensional because it employs sources and observations in different directions/dimensions. $\hat{\mathbf{W}}$ contains the sought for $\hat{W}_{in}(\mathbf{x}_R, \mathbf{x})$, which can be addressed as virtual-source responses as they are obtained without using sources at $\mathbf{x}$. It should be noted that, even if physical sources were available, the $\hat{W}_{in}(\mathbf{x}_R, \mathbf{x})$ could not be directly measured because the propagators are artificial ones (in fact, the modal scaling by $\hat{B}_v$ makes them unnatural; see eq. 23). Still, the virtual-source responses can be retrieved from real observations (as expressed by eq. 36), and they can be modelled using the well-defined expression given in eq. (23).

In acoustics, the point-spread function converges to a band-limited spike in space and time when there is a perfect distribution of sources around the receivers whose observations are correlated (in that case, MDD does not improve the CC result, unless there are losses; Wapenaar *et al.* 2011b). We note, however, that the current point-spread functions are necessarily distributed/broad in space. The reason is that the considered surface wave response (eq. 3) is a far-field approximation. It assumes that the surface waves have a fully developed depth profile and only propagate horizontally. Therefore, all functions in eq. (31) (*cf.* eqs 23, 32 and 33) are necessarily distributed in depth direction (even for zero horizontal offset); in Appendix B, we verify this mathematically for the point-spread functions related to surface waves in a homogeneous half-space with a perfect distribution of sources. Eq. (36) thus expresses that the depth profile of the propagators is obtained by correcting the depth profiles of the correlation functions and those of the point-spread functions. This correction can be significant, depending on the distribution of the sources (as discussed earlier).

The above-introduced matrix $\hat{\mathbf{\Upsilon}} = \hat{\mathbf{\Upsilon}}(z, z', \omega)$ can be used to diagnose the quality of the MDD process. The matrix consists of four separate matrices $\hat{\mathbf{\Upsilon}}_{xx}$, $\hat{\mathbf{\Upsilon}}_{xz}$, $\hat{\mathbf{\Upsilon}}_{zx}$ and $\hat{\mathbf{\Upsilon}}_{zz}$. In the ideal case where the inversion does not need to be stabilized and $\hat{\mathbf{\Gamma}}\hat{\mathbf{\Gamma}}^{-1} \rightarrow \mathbf{I}$, which is the case when surface S (eq. 31) is covered by a dense line of receivers and when there is a densely-sampled source line in depth direction, $\hat{\mathbf{\Upsilon}}_{xx}, \hat{\mathbf{\Upsilon}}_{zz} \rightarrow \mathbf{I}$ and $\hat{\mathbf{\Upsilon}}_{xz}, \hat{\mathbf{\Upsilon}}_{zx} \rightarrow \mathbf{O}$ for all ω. This implies that the corresponding functions $\Upsilon_{xx}(z, z', t)$ and $\Upsilon_{zz}(z, z', t)$ have a spike in space and time (i.e. a band-limited Dirac function), and that $\Upsilon_{xz}(z, z', t)$ and $\Upsilon_{zx}(z, z', t)$ approach zero. The Υ_{xx} and Υ_{zz} could therefore be interpreted to capture the distributions of the virtual-source components after MDD, as it is done in acoustics and elastodynamics when dealing with body waves (van der Neut *et al.* 2011; Wapenaar *et al.* 2011b). This still holds true for the temporal distribution in the current surface wave problem. However, as the depth profile of the propagators $\hat{W}_{in}(\mathbf{x}_R, \mathbf{x})$ is necessarily broad (as discussed above), it might be confusing to refer to the Υ_{xx} and Υ_{zz} as if they capture the spatial distributions of the virtual-source components. The spatial distributions of the Υ_{xx} and Υ_{zz} just indicate how well the depth profiles of the $\hat{W}_{in}(\mathbf{x}_R, \mathbf{x})$ are obtained after the MDD process.

We emphasize that the proposed MDD scheme is not restricted to cylindrical configurations. We used the cylindrical volume V for simplicity (*cf.* Sections 2 and 3); the integral over S could be easily evaluated using cylindrical coordinates and the stationary-phase approximation. In general, however, it is important that the receivers at S do sample the stationary point that lies in the plane of $\mathbf{x}_S$ and $\mathbf{x}_R$, but the specific shape of S is of minor importance. Furthermore, it is probably easiest to have sources at only one side of V in applications. Then, in 2-D, a single array of receivers is sufficient (half of the surface S), and the inward-propagating field is simply the total field. Otherwise, decomposition into inward- and outward-propagating waves might be required.

To facilitate comparison of the results obtained using the MDD and CC methods (Section 5), we indicate here how the virtual-source responses in the latter method can be estimated using the correlation integrals in eq. (20). In practical applications, all modes are taken together, and the modal scale factors $\hat{A}_v$ are ignored as they are unknown; only the time derivative is applied. The resulting expressions are very similar to the correlation functions (eq. 32; for the integrals, stricter sampling criteria hold). The virtual-source responses of the CC method can then be estimated as

$$\hat{u}_{ik}(\mathbf{x}_R, \mathbf{x}') \cong \hat{G}_{ik}(\mathbf{x}_R, \mathbf{x}')\hat{P} \cong -\mathrm{i}\omega\hat{C}_{ik}(\mathbf{x}_R, \mathbf{x}'). \tag{37}$$

Here, the $\hat{u}_{ik}$ are displacements and $\hat{P}$ is some average power spectrum of the sources (Wapenaar & Fokkema 2006), indicating that band-limited Green's functions are retrieved. The estimated virtual-source responses obtained from the correlation functions can be poor due to a lack of sources, their non-uniform distribution, or due to the missing modal scale factors of the correlation integral. In the current MDD scheme, we also have unknown modal scale factors, but they are incorporated in the propagators (eq. 23). Hence, they are part of the solution we are looking for, and not knowing them beforehand does not influence the quality of the retrieved virtual-source responses.

Finally, we note that the current method of retrieving a virtual-source response by MDD is different from that in Slob *et al.* (2007) and Halliday & Curtis (2009). In these papers, the retrieved virtual-source response is based on (cross-)convolution, which is similar to the conventional CC method, but based on the convolution-type reciprocity theorem. Like the current method, the convolutional method also works for retrieving surface waves in lossy media, but it requires having sources between the virtual source and the receiver(s) (*cf.* Fig. 2). It also requires a regular distribution of sources, while MDD can handle non-uniform illumination (and compensate for the associated artefacts in the CC method; Wapenaar *et al.* 2011b). To accomplish this, an array of receivers is required (along S; *cf.* Fig. 2), while the convolutional method only needs two receivers (like the CC method).

5 NUMERICAL RESULTS

In this section, we show numerical examples to verify the performance of the MDD scheme and compare the retrieved virtual-shot responses with those obtained using the CC method. We compare the distributions of the associated virtual sources and analyse the required length of the vertical array needed to compute the point-spread functions. We restrict to a 2-D situation in view of the envisaged applications of the MDD scheme (see also Section 6).

To ensure relatively strong higher mode surface waves, we chose to consider the layered medium used by Halliday & Curtis (2008, see Table 1). We modelled band-limited surface wave responses (10 Hz Ricker pulse for all sources) due to five sources distributed at the surface, with 34 receivers along S (in vertical direction) and 81 receivers $\mathbf{x}_R$ at the surface(see Fig. 3, where also the sampling intervals are indicated). The propagation distances between the sources and S, and between S and the receivers $\mathbf{x}_R$ were chosen so that the

Table 1. Subsurface layering and corresponding material parameters taken from Halliday & Curtis (2008): compressional wave speed c_P, shear wave speed c_S and material density ρ.

Depth (m)	c_P (m s^{-1})	c_S (m s^{-1})	ρ (kg m^{-3})
0–1	404	101	1400
1–2	504	126	1460
2–4	508	127	1470
4–6	584	146	1520
6–8	688	172	1590
8–12	736	184	1610
12–20	800	200	1650
20–30	928	232	1710
>30	1228	307	1840

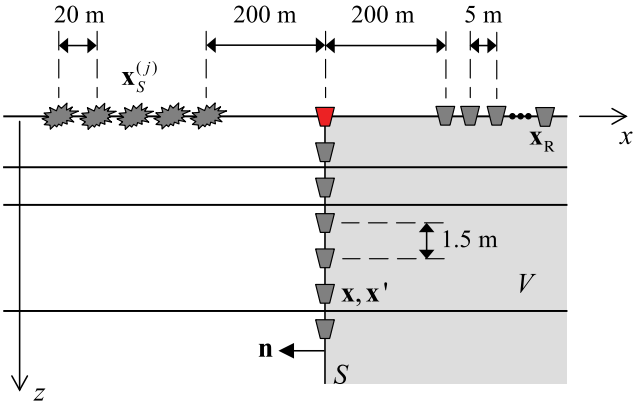

Figure 3. 2-D configuration for the numerical experiments described in Section 5. The virtual source lies at the surface and is indicated by the red receiver.

far-field criterion is fulfilled, which is required for the use of the surface wave response in eq. (3). For modelling of the 2-D responses, we used the 3-D responses as in eq. (3), which were computed numerically (Hisada 1994; Lai & Rix 1998), and applied the following conversion (Aki & Richards 2002):

$$\hat{G}^{\nu,\mathrm{2D}}_{nm}(\mathbf{x},\mathbf{x}_S) = \sqrt{\frac{2\pi\xi_S}{k_\nu}}\,\mathrm{e}^{-\mathrm{i}\frac{\pi}{4}}\,\hat{G}^{\nu,\mathrm{3D}}_{nm}\left(\mathbf{x}|_{y=0},\mathbf{x}_S|_{y_S=0}\right). \tag{38}$$

For the considered finite frequency band, the responses contain a finite number of modes ν. The length of the vertical array was chosen so that, at the centre frequency of the source, the involved modal eigenfunctions associated with the highest mode (which has the largest depth penetration) are decayed over 95 per cent (see Appendix A for modal eigenfunctions), indicating that the surface waves have practically vanished at this depth.

We computed all required components (for $i, k, n = \{x, z\}$; see eqs 31–33) to form the correlation and point-spread matrices. Because the medium is laterally invariant (no scattering), the inward-propagating fields are the same as the total fields at the left part of S. The right part can be ignored (fields are outgoing there), so that only one vertical array suffices. We subsequently applied singular-value decomposition to compute the inverse of the point-spread matrix, which has to be done for each of the frequencies separately; to stabilize the inversion (Menke 1989; Minato *et al.* 2011), we omitted the very small singular values (see also Section 4). The virtual-source responses were obtained using eq. (36). In all numerical results that we discuss in this section, the virtual source $\mathbf{x}$ is located at the surface and indicated by the red receiver in Fig. 3. In particular, we discuss the band-limited responses $w_{zz}(\mathbf{x}_R, \mathbf{x}, t)$ (MDD)

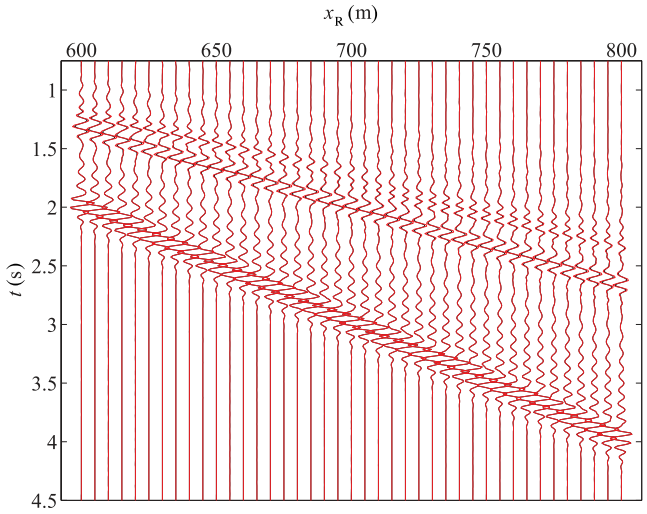

Figure 4. Virtual-shot record $w_{zz}(\mathbf{x}_R, \mathbf{x}, t)$ retrieved using the MDD scheme (black line) and the directly modelled response (red line); both responses have been normalized. The lines overlie to a large extent. We used five surface sources and 34 receivers along S with 1.5 m spacing. The first receiver is located at $\mathbf{x}_R = [600, 0]^T$. For clarity, not all 81 traces are shown.

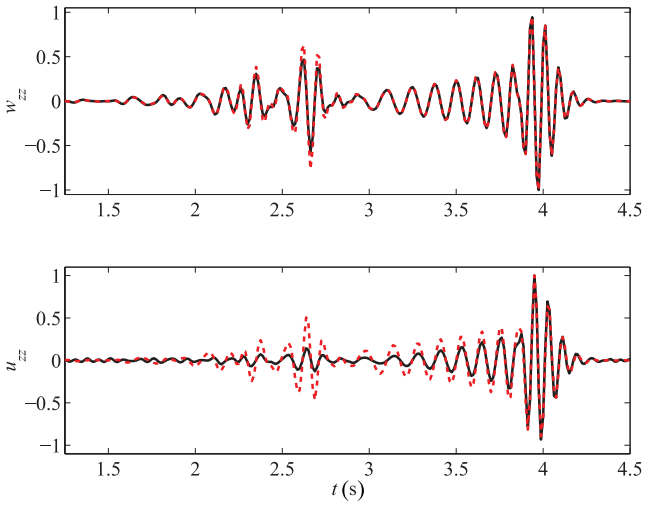

Figure 5. Retrieved (black line) virtual-shot responses w_{zz} (MDD; upper panel) and u_{zz} (CC; lower panel), together with the directly modelled responses (red dashed lines); all responses have been normalized. We used five surface sources and 34 receivers along S with 1.5 m spacing. The receiver is located at $\mathbf{x}_R = [800, 0]^T$.

and $u_{zz}(\mathbf{x}_R, \mathbf{x}', t)$ (CC), where the former is obtained by convolving $W_{zz}(\mathbf{x}_R, \mathbf{x}, t)$ with $P(t)$; $P(t)$ is the zero-phase pulse corresponding to the power spectrum of the employed sources, which is taken the same as in the CC method for fair comparison (see eq. 37). Furthermore, the location of the virtual source in the CC method is denoted as $\mathbf{x}'$ rather than $\mathbf{x}$, but that is only a different notation for the same points in space (see Section 4).

The retrieved virtual-shot record w_{zz} (MDD) is shown in Fig. 4 together with the directly modelled result (from eq. 23 for a source at the virtual-shot position). Apparently, the retrieval is quite accurate (the same is true for the other components). All surface wavemodes are properly retrieved, and spurious events cannot be distinguished. The only error is in amplitude, which is confirmed by Fig. 5 (upper panel), where a single-offset virtual-shot response is shown; the phase is correct and the waveform is the same as that of the directly

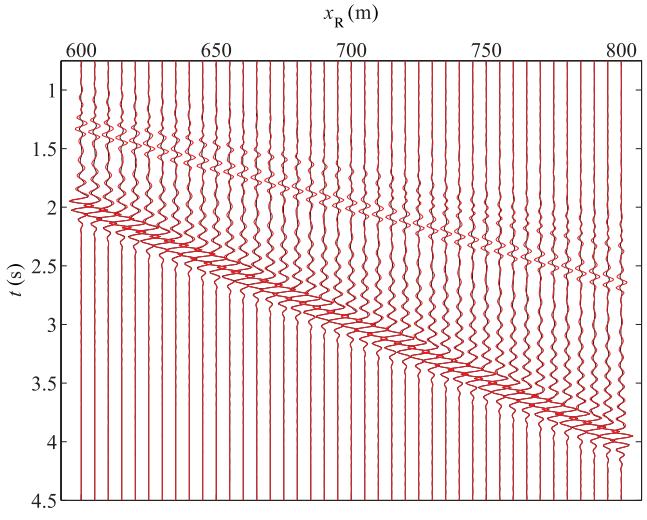

Figure 6. Virtual-shot record $u_{zz}(\mathbf{x}_R, \mathbf{x}', t)$ retrieved using the CC method (black line) and the directly modelled response (red line); both responses have been normalized. We used five surface sources. The first receiver is located at $\mathbf{x}_R = [600, 0]^T$. For clarity, not all 81 traces are shown.

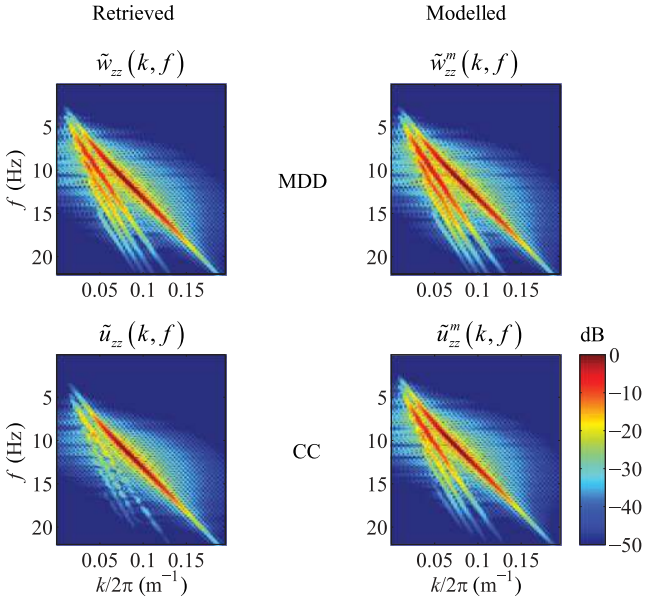

Figure 7. The k, f-domain spectra of the retrieved and directly modelled responses $\tilde{w}_{zz}$ and $\tilde{u}_{zz}$ ('m' refers to directly modelled responses); dB refers to normalized response [i.e. $20\log_{10}(\dots)$ of normalized k, f-domain responses]. We used five surface sources and 34 receivers along S with 1.5 m spacing. Note that $\tilde{w}_{zz}(k, f) = \tilde{w}_{zz}(k, z_R, \mathbf{x}, f)$ and $\tilde{u}_{zz}(k, f) = \tilde{u}_{zz}(k, z_R, \mathbf{x}', f)$.

modelled response. Using another numerical simulation with five sources along a vertical line and 2.5 m spacing, we verified that the amplitude error is not caused by missing subsurface sources (the result is not shown here). Therefore, we conclude that the amplitude difference is a result of the ignored cross terms (Section 4). Even in the case of relatively strong higher modes, ignoring the cross terms thus only affects the retrieved amplitude.

The retrieved u_{zz} (CC; eq. 37) is less accurate, as can be seen from Figs 5 (lower panel) and 6 [where eq. 3 was used for the directly modelled response, with a source of signature $P(t)$ at the virtual-shot position and a receiver at $\mathbf{x}_R$]. Though spurious events cannot be observed in the latter figure, the amplitude mismatch is stronger, and there is some phase error for the higher modes (see Fig. 5: around $t = 2$ s). This confirms the findings of Halliday & Curtis (2008) and Kimman & Trampert (2010). Spurious events are suppressed due to the applied source configuration, which approaches a homogeneous surface-source distribution.

The wavenumber–frequency (k, f) spectra can be calculated using the Fourier transform over t (eq. 1) and over x_R (receiver array), where the latter is defined as [similarly for $\hat{u}_{zz}(\mathbf{x}_R, \mathbf{x}, \omega)$]

$$\tilde{w}_{zz}(k, z_R, \mathbf{x}, \omega) = \int_{-\infty}^{\infty} \hat{w}_{zz}(\mathbf{x}_R, \mathbf{x}, \omega) \exp(\mathrm{i}kx_R)\, \mathrm{d}x_R. \tag{39}$$

Here, k denotes the angular horizontal wavenumber and the tilde refers to the $(k, z_R, \mathbf{x}, \omega)$ domain. The spectra of the retrieved $\tilde{w}_{zz}$ and $\tilde{u}_{zz}$ are shown in Fig. 7, together with the directly modelled equivalents. The higher mode surface waves are clearly present, and their cut-off frequencies can even be distinguished. As we expect based on the previous results, the retrieved $\tilde{w}_{zz}$ looks very similar to the true one; all modes are nicely retrieved. The quality of the retrieved $\tilde{u}_{zz}$ is less high. In particular, the higher modes cannot be distinguished that well. This is due to the lack of subsurface sources (Halliday & Curtis 2008; Kimman & Trampert 2010) and due to the small amplitudes (Fig. 6), which is related to the missing modal scale factors (of the correlation integral).

To assess subsurface properties, dispersion analyses of surface waves are often performed. For a dispersion analysis using k, f-domain spectra, where the frequency-dependent phase velocities are picked from the energy maxima (Gabriels *et al.* 1987), the MDD result is clearly preferable and will give reliable results. When only one or a few different virtual-shot responses are present, and the Fourier transform over x_R cannot be applied, it is very important that the retrieved waveform has the proper phase; errors in the phase can significantly affect the estimated phase velocity when based on a single-offset response (Bensen *et al.* 2007; Kimman & Trampert 2010; Ruigrok 2012). Group velocities, which are often estimated using the envelope function of an analytic signal, also suffer from phase errors (e.g. Bensen *et al.* 2007).

We can verify that the results obtained using the MDD scheme are very similar when we use a shorter array consisting of 20 receivers along S with the same spacing (the results are not shown here). The amplitude of the fastest modes is then retrieved with a small amplitude error, which is related to the fact that the surface wave eigenfunctions are not fully decayed at the deepest receiver, but the phase is still correct. Shorter arrays can thus be used, but there is a trade-off. For example, once we take six receivers along S, phase errors are obtained for the fastest modes. In addition, to suppress amplitude errors, more singular values need to be omitted in computing the inverse of $\hat{\mathbf{\Gamma}}$. It effectively reduces the bandwidth in which useful signal is retrieved. This is the most significant when only one receiver is used at S (at the surface), the results of which are displayed in Figs 8 and 9. In the latter figure, it can be seen that some high-frequency information is lost, particularly for the higher modes. However, the MDD result is still better than the CC result. In general, the lower accuracy of the current MDD result compared to that having 34 receivers along S is a consequence of not having a proper array needed for the integral in eq. (31), and of cross terms that might become stronger for shorter arrays since the orthogonality is less well approximated (*cf.* Sections 2 and 3).

The point-spread function $\Gamma_{zz}(z, z', t)$ associated with the example having 34 receivers along S is shown in Fig. 10; both its spatial and the temporal distributions are displayed ($z' = 0$ because the virtual source lies at the surface, as explained above; see also Fig. 3).

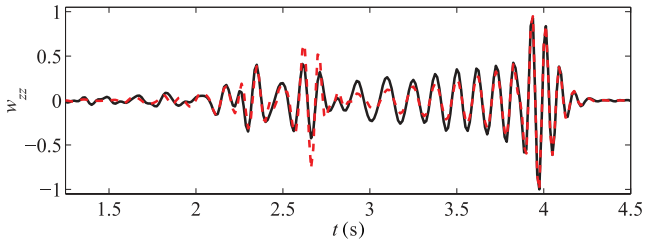

Figure 8. Retrieved (black line) virtual-shot response w_{zz} (MDD), together with the directly modelled response (red dashed line); both responses have been normalized. We used five surface sources and one surface receiver at S. The receiver is located at $\mathbf{x}_R = [800, 0]^T$. The associated $\tilde{u}_{zz}$ (CC) is the same as in Fig. 5.

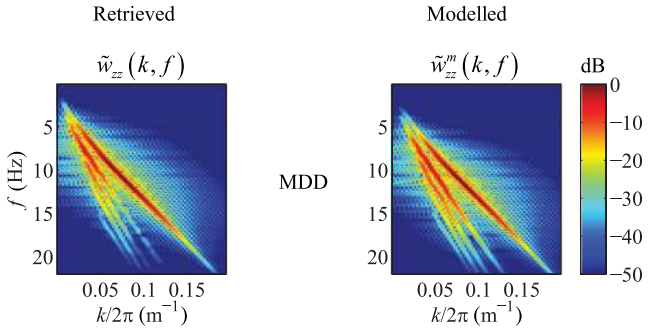

Figure 9. The k, f-domain spectra of the retrieved and directly modelled responses $\tilde{w}_{zz}$ and $\tilde{u}_{zz}$ ('m' refers to directly modelled responses); dB refers to normalized response (*cf.* Fig. 7). We used five surface sources and one surface receiver at S. Note that $\tilde{w}_{zz}(k, f) = \tilde{w}_{zz}(k, z_R, \mathbf{x}, f)$. The associated CC results are the same as in Fig. 7.

Apparently, Γ_{zz} is distributed in space and time. The fact that it is broad in space is not only caused by the non-uniform illumination, like for body waves (Wapenaar *et al.* 2011b), but is an intrinsic property of the point-spread function, even for ideal source geometries (see Section 4 and Appendix B). The temporal distribution, however, is not necessarily broad. In this case, it is quite localized

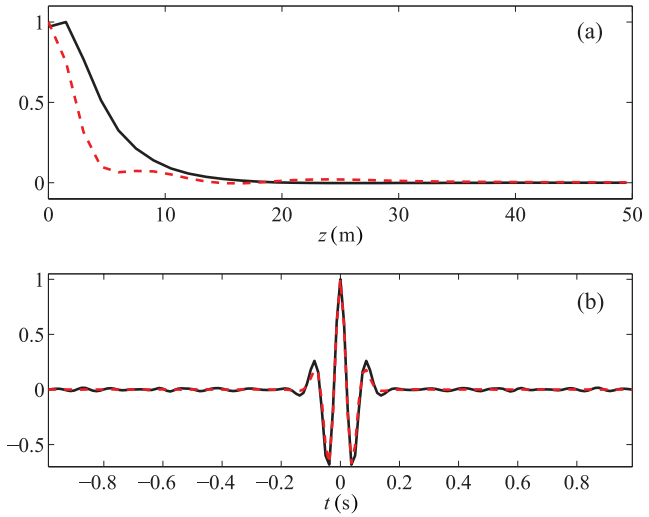

Figure 10. Normalized spatial and temporal distributions of the point-spread function Γ_{zz} (black line) and of Υ_{zz} (defined in text; red dashed line). Panel (a): $\Gamma_{zz}(z, z', t)|_{z'=0,t=0}$ and $\Upsilon_{zz}(z, z', t)|_{z'=0,t=0}$; panel (b): $\Gamma_{zz}(z, z', t)|_{z=0,z'=0}$ and $\Upsilon_{zz}(z, z', t) * P(t)|_{z=0,z'=0}$ [$P(t)$ is defined in the text]. We used five surface sources and 34 receivers along S with 1.5 m spacing.

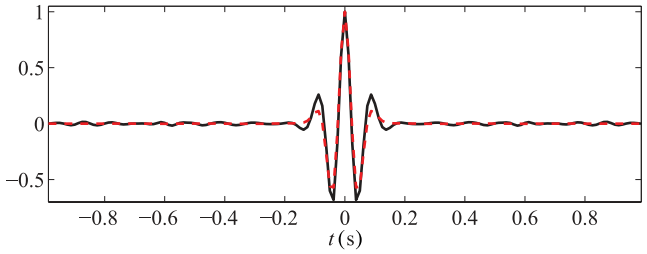

Figure 11. Normalized temporal distributions of the point-spread function Γ_{zz} (black line) and of Υ_{zz} (defined in text; red dashed line): $\Gamma_{zz}(t)$ and $\Upsilon_{zz}(t) * P(t)$ [$P(t)$ is defined in the text]. We used five surface sources and one surface receiver at S. $\Gamma_{zz}(t)$ is the same as in Fig. 10, but included for comparison.

due to the applied surface source distribution, which gives relatively good CC results (Halliday & Curtis 2008). We can verify that the temporal smearing is much larger when we only incorporate two surface sources (result not shown here). In Fig. 10, we also display $\Upsilon_{zz}(z, z', t)$, being an indicator of the quality of the retrieved w_{zz} (see Section 4); we convolved the function with $P(t)$ to facilitate comparison with the point-spread function Γ_{zz}. As expected, Υ_{zz} has a band-limited spike in space. The temporal spike is obviously modified by the zero-phase pulse, but the obtained function is better localized in time than Γ_{zz}. Though the difference is not so large, it indicates that the virtual source response obtained using MDD has higher quality than that obtained using the CC method. This confirms the results in Figs 5 and 7.

The functions $\Gamma_{zz}(t)$ and $\Upsilon_{zz}(t)$ associated with the extreme case of only one surface receiver at S are shown in Fig. 11. These functions only depend on time; their spatial distributions are not defined as they can only be computed at one location. The corresponding deconvolution is therefore only a temporal one. It is clear from Fig. 11 that the deconvolution still sharpens up the distribution of the virtual source (though only in time), which once more confirms the improved result after MDD (Figs 8 and 9) compared to the CC method (Figs 5 and 7).

6 DISCUSSION

Here, we make a connection of the current MDD scheme with that used by Wapenaar *et al.* (2011a). In addition, we discuss the applicability in practical situations where the proposed MDD scheme can be used for improved surface wave retrieval.

Wapenaar *et al.* (2011a) successfully performed MDD, using a scalar (single-component) scheme for the specific situation of only having the fundamental-mode surface wave present in the responses and only surface receivers to compute a point-spread function. In fact, the surface wave was treated as a scalar wave that travels in the surface (x, y) plane. The retrieved result using the scalar scheme is, in principle, exact for an ideal surface receiver array and ideal illumination. Using the current elastic (multicomponent) scheme and choosing only a single surface receiver at S, MDD can be applied in a similar way (taking only the fundamental mode in the modelling); the only difference is that we do not incorporate the y-direction. The results are of slightly less quality than those of the scalar scheme. The waveform of w_{zz} is retrieved quite well, as shown in Fig. 12, but there is some phase error at the onset of the signal. Apparently, particularly the lower frequencies suffer from the lack of receivers at depth that are required for the elastic scheme (eq. 31). It is interesting to note that the MDD result has similar quality as that obtained using the CC method (see also Fig. 12. We

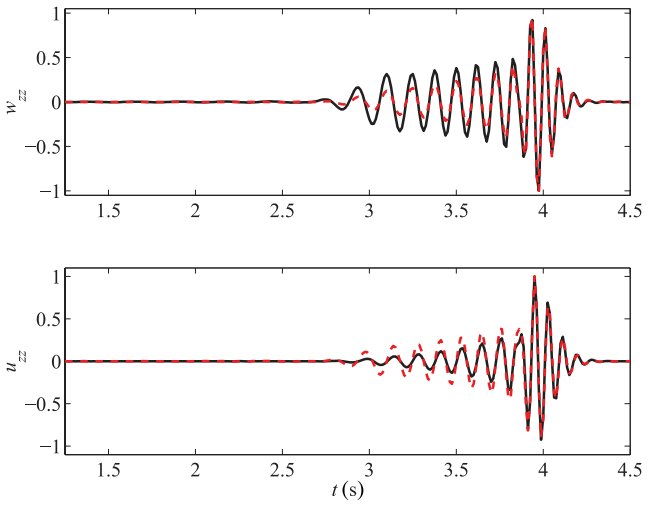

Figure 12. Retrieved (black line) fundamental-mode virtual-shot responses w_{zz} (MDD; upper panel) and $\tilde{u}_{zz}$ (CC; lower panel), together with the directly modelled responses (red dashed lines); all responses have been normalized. We used five surface sources and one surface receiver at S. The receiver is located at $\mathbf{x}_R = [800, 0]^T$.

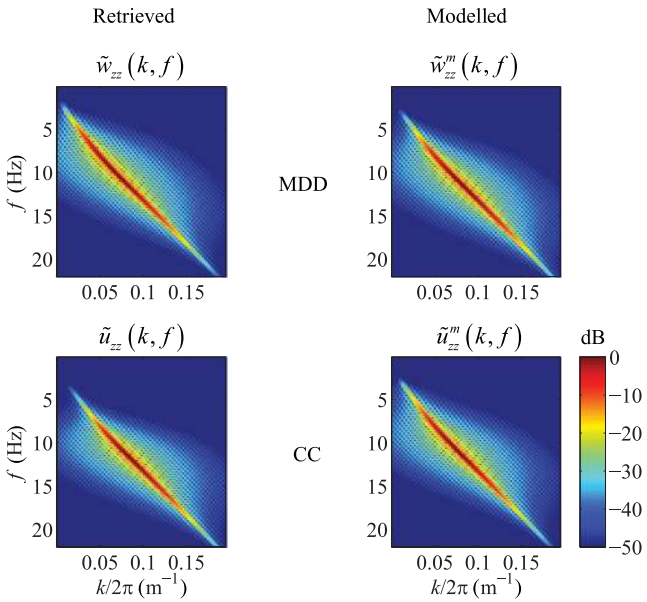

Figure 13. The k, f-domain spectra of the retrieved and directly modelled fundamental-mode responses $\tilde{w}_{zz}$ and $\tilde{u}_{zz}$ ('m' refers to directly modelled responses); dB refers to normalized response (*cf.* Fig. 7). We used five surface sources and one surface receiver at S. Note that $\tilde{w}_{zz}(k, f) = \tilde{w}_{zz}(k, z_R, \mathbf{x}, f)$ and $\tilde{u}_{zz}(k, f) = \tilde{u}_{zz}(k, z_R, \mathbf{x}', f)$.

can verify that the CC result does not get much better when 10 regularly distributed sources are used; hence, the current result seems to be the best we can get). Therefore, for this specific situation, using MDD is only advantageous when one has to cope with non-uniform illumination in lateral (y) direction (which is exactly the case in Wapenaar *et al.* 2011a) or with losses. Furthermore, it is clear from Fig. 13 that the dispersion curves can be retrieved reliably, both for the MDD and CC methods. Dispersion analyses are thus expected to give accurate results as long as they are based on the k, f-domain responses.

We envisage different applications of the proposed elastic MDD scheme. When only surface receivers are present, the elastic scheme can be used for multimode surface waves (*cf.* Figs 8 and 9); for single-mode surface waves, the scalar scheme of Wapenaar *et al.* (2011a) gives superior results (as described earlier). For getting better accuracy in retrieving the higher modes using subsurface receivers, we envisage applications of the elastic scheme mainly in 2-D, where only one vertical array is required. A large set of boreholes to enable a 3-D application of the scheme is probably too costly. A 2-D application is reasonable when the available ambient noise source approximates a line source (e.g. a shore line), or when a line source can be created by having active sources along a line in lateral direction (the successively recorded responses should then be stacked). Nowadays, subsurface arrays are applied more and more. Bakulin *et al.* (2012) use buried arrays for seismic monitoring of deep targets on land. Using the recently developed seismic cone penetrometer (Ghose 2012), a shallow vertical array can be made relatively easy in soft soil. Instrumented boreholes have become available as well. One large-scale example is the pilot borehole close to San Andreas Fault in California for monitoring purposes (Chavarria *et al.* 2004); it has a 1240-m long array of 40-m spaced sensors.

Depending on the scale, the MDD scheme can be used for different purposes. In our opinion, possible applications are: dispersion analysis used for estimating shallow-subsurface properties (e.g. shear velocity profile; Wathelet *et al.* 2004), monitoring of the shallow subsurface, and suppressing surface waves from seismic data to enable investigation of deeper targets using body waves (e.g. Halliday *et al.* 2007, 2010; Bakulin *et al.* 2012). Especially for the latter two applications, an important advantage of the MDD scheme is that it can cope with different source signatures and source-to-ground coupling differences (for the 2-D application, at least in in-line direction). Source repeatability constraints are thus relaxed compared to the CC method.

7 CONCLUSIONS

Virtual-source surface wave responses can be reconstructed using the CC of the observed wavefields at two receivers. When there is a lack of subsurface sources, which is often the case in practical situations, especially higher mode surface waves cannot be properly retrieved from the observations.

The aim of this paper was to apply MMD for improving the retrieval of the surface wave response. We proposed an approximate convolution theorem for forward propagation of surface waves in layered media that are laterally invariant (no scattering), and we determined the involved modal scale factors using a stationary-phase analysis. Based on the proposed theorem, we derived an MDD scheme for the retrieval of surface waves. In fact, the scheme introduces an additional processing step compared to the CC method; the result of the latter is deconvolved by a so-called point-spread tensor. The involved point-spread functions capture the imprint of the non-uniform illumination (i.e. the lack of subsurface sources) and possible anelastic effects, and quantify the associated smearing of the virtual-source components. Using a 2-D example, we found that the MDD scheme partially corrects for this undesired smearing and that the retrieved surface wave response, including the higher modes, becomes more accurate. In the ideal situation, where the depth of the required vertical array is equal to the depth penetration of the surface waves, there is only some amplitude difference compared to the directly modelled surface wave response; this difference is due to ignored cross-mode terms in the approximate convolution theorem. Shorter arrays are also possible. In the limit case of only

a single surface receiver, the retrieved virtual-source response obtained using MDD is still more accurate than the corresponding CC result.

The required point-spread functions can be calculated from the same wavefields as used in the CC method. For the envisaged line-source applications, the scheme requires one shallow vertical array of multicomponent geophones. Furthermore, the scheme employs exclusively multicomponent point-force responses rather than their spatial derivatives, which is advantageous for applications with contemporary field-acquisition geometries. Finally, it can cope with differences in source spectra and source-to-ground coupling, and gives accurate results when only surface sources are available. We expect that the improved retrieval of multimode surface waves can facilitate dispersion analyses in shallow-subsurface inversion problems and monitoring, and surface wave removal algorithms.

ACKNOWLEDGEMENTS

We thank Joost van der Neut for giving valuable comments. Furthermore, we thank Andrew Curtis and an anonymous reviewer for their valuable suggestions to improve the manuscript. This research is sponsored by The Netherlands Research Centre for Integrated Solid Earth Sciences (ISES).

REFERENCES

Achenbach, J.D., 1973. *Wave Propagation in Elastic Solids,* North–Holland Publishing Company.

Aki, K. & Richards, P.G., 2002. *Quantitative Seismology,* Freeman & Co.

Bakulin, A. & Calvert, R., 2006. The virtual source method: theory and case study, *Geophysics,* **71,** SI139–SI150.

Bakulin, A., Burnstad, R., Jervis, M. & Kelamis, P., 2012. Evaluating permanent seismic monitoring with shallow buried sensors in a desert environment, SEG Technical Program Expanded Abstracts 2012, pp. 1–5.

Beaty, K.S., Schmitt, D.R. & Sacchi, M., 2002. Simulated annealing inversion of multimode Rayleigh wave dispersion curves for geological structure, *Geophys. J. Int.,* **151,** 622–631.

Bensen, G.D., Ritzwoller, M.H., Barmin, M.P., Levshin, A.L., Lin, F., Moschetti, M.P., Shapiro, N.M. & Yang, Y., 2007. Processing seismic ambient noise data to obtain reliable broad-band surface wave dispersion measurements, *Geophys. J. Int.,* **169,** 1239–1260.

Campillo, M. & Paul, A., 2003. Long-range correlations in the diffuse seismic coda, *Science,* **299,** 547–549.

Chavarria, J.A., Malin, P.E. & Shalev, E., 2004. The SAFOD Pilot Hole seismic array: wave propagation effects as a function of sensor depth and source location, *Geophys. Res. Lett.,* **31,** L12S07, doi:10.1029/2003GL019382.

de Hoop, A.T., 1995. *Handbook of Radiation and Scattering of Waves,* Academic Press.

Dost, B., 1990. Upper mantle structure under western Europe from fundamental and higher mode surface waves using the NARS array, *Geophys. J. Int.,* **100,** 131–151.

Draganov, D., Wapenaar, K., Mulder, W., Singer, J. & Verdel, A., 2007. Retrieval of reflections from seismic background-noise measurements, *Geophys. Res. Lett.,* **34,** L04305, doi:10.1029/2006GL028735.

Drijkoningen, G.G., Rademakers, F., Slob, E.C. & Fokkema, J.T., 2006. A new elastic model for ground coupling of geophones with spikes, *Geophysics,* **71,** Q9–Q17.

Gabriels, P., Snieder, R. & Nolet, G., 1987. In situ measurement of shear-wave velocity in sediments with higher-mode Rayleigh waves, *Geophys. Prospect.,* **35,** 187–196.

Gerstoft, P., Sabra, K.G., Roux, P., Kuperman, W.A. & Fehler, M.C., 2006. Green's functions extraction and surface-wave tomography from microseisms in southern California, *Geophysics,* **71,** SI23–SI31.

Ghose, R., 2012. A microelectromechanical system digital 3C array seismic cone penetrometer, *Geophysics,* **77,** WA99–WA107.

Halliday, D. & Curtis, A., 2008. Seismic interferometry, surface waves and source distribution, *Geophys. J. Int.,* **175,** 1067–1087.

Halliday, D. & Curtis, A., 2009. Seismic interferometry of scattered surface waves in attenuative media, *Geophys. J. Int.,* **178,** 419–446.

Halliday, D.F., Curtis, A., Robertsson, J.O.A. & van Manen, D.-J., 2007. Interferometric surface-wave isolation and removal, *Geophysics,* **72,** A69–A73.

Halliday, D., Curtis, A., Vermeer, P., Strobbia, C., Glushchenko, A., van Manen, D.-J. & Robertsson, J.O.A., 2010. Interferometric ground-roll removal: attenuation of direct and scattered surface waves in single-sensor data, *Geophysics,* **75,** SA15–SA25.

Hisada, Y., 1994. An efficient method for computing Green's functions for a layered half-space with sources and receivers at close depths, *Bull. seism. Soc. Am.,* **84**(5), 1456–1472.

Jeffreys, H. & Jeffreys, B.S., 1946. *Methods of Mathematical Physics,* Cambridge Univ. Press.

Kimman, W.P. & Trampert, J., 2010. Approximations in seismic interferometry and their effects on surface waves, *Geophys. J. Int.,* **182,** 461–476.

Lai, C.G. & Rix, G.J., 1998. Simultaneous inversion of Rayleigh phase velocity and attenuation for near-surface site characterization. Report No. GIT-CEE/GEO-98-2, School of Civil and Environmental Engineering, Georgia Institute of Technology.

Larose, E. *et al.*, 2006. Correlation of random wavefields: an interdisciplinary review, *Geophysics,* **71,** SI11–SI21.

Louie, J.N., 2001. Faster, better: shear-wave velocity to 100 meters depth from refraction microtremor arrays, *Bull. seism. Soc. Am.,* **91,** 347–364.

MacBeth, C.D. & Burton, P.W., 1985. Upper crustal shear velocity models from higher mode Rayleigh wave dispersion in Scotland, *Geophys. J. R. astr. Soc.,* **83,** 519–539.

Menke, W., 1989. *Geophysical Data Analysis: Discrete Inverse Theory,* Academic Press.

Minato, S., Matsuoka, T., Tsuji, T., Draganov, D., Hunziker, J. & Wapenaar, K., 2011. Seismic interferometry using multidimensional deconvolution and crosscorrelation for crosswell seismic reflection data without borehole sources, *Geophysics,* **76,** SA19–SA34.

Nolet, G. & Panza, G.F., 1976. Array analysis of seismic surface waves: limits and possibilities, *Pageoph,* **114**(5), 775–790.

Park, C.B., Miller, R.D., Xia, J. & Ivanov, J., 2007. Multichannel analysis of surface waves (MASW)—active and passive methods, *Leading Edge,* **26,** 60–64.

Ruigrok, E.N., 2012. Body-wave seismic interferometry applied to earthquake- and storm-induced wavefields, *PhD thesis,* Delft University of Technology, Delft.

Schuster, G.T., 2009. *Seismic Interferometry,* Cambridge Univ. Press.

Shapiro, N.M., Campillo, M., Stehly, L. & Ritzwoller, M.H., 2005. High-resolution surface-wave tomography from ambient seismic noise, *Science,* **175,** 1615–1618.

Slob, E., Draganov, D. & Wapenaar, K., 2007. Interferometric electromagnetic Green's functions representations using propagation invariants, *Geophys. J. Int.,* **169,** 60–80.

Snieder, R., 2002. Scattering of surface waves, in *Scattering and Inverse Scattering in Pure and Applied Science,* pp. 562–577, eds Pike, R. & Sabatier, P., Academic Press.

Snieder, R., 2004. Extracting the Green"s function from the correlation of coda waves: a derivation based on stationary phase, *Phys. Rev. E,* **69,** 046610, doi:10.1103/PhysRevE.69.046610.

Snieder, R., Miyazawa, M., Slob, E., Vasconcelos, I. & Wapenaar, K., 2009. A comparison of strategies for seismic interferometry, *Surv. Geophys.,* **30,** 503–523.

van der Neut, J., Thorbecke, J., Mehta, K., Slob, E. & Wapenaar, K., 2011. Controlled-source interferometric redatuming by crosscorrelation and multidimensional deconvolution in elastic media, *Geophysics,* **76,** SA63–SA76.

Wapenaar, C.P.A. & Berkhout, A.J., 1989. *Elastic Wave Field Extrapolation,* Elsevier.

Wapenaar, K. & Fokkema, J., 2006. Green's function representations for seismic interferometry, *Geophysics,* **71,** SI33–SI46.

Wapenaar, K., Ruigrok, E., van der Neut, J. & Draganov, D., 2011. Improved surface-wave retrieval from ambient seismic noise by multi-dimensional deconvolution, *Geophys. Res. Lett.,* **38,** L01313, doi: 10.1029/2010GL045523.

Wapenaar, K., van der Neut, J., Ruigrok, E., Draganov, D., Hunziker, J., Slob, E., Thorbecke, J. & Snieder, R., 2011. Seismic interferometry by crosscorrelation and by multidimensional deconvolution: a systematic comparison, *Geophys. J. Int.,* **185,** 1335–1364.

Wathelet, M., Jongmans, D. & Ohrnberger, M., 2004. Surface-wave inversion using a direct search algorithm and its application to ambient vibration measurements, *Near Surf. Geophys.,* **2,** 211–221.

Xia, J., Miller, R.D. & Park, C.B., 1999. Estimation of near-surface shear-wave velocity by inversion of Rayleigh waves, *Geophysics,* **64,** 691–700.

Xia, J., Miller, R.D., Park, C.B. & Tian, G., 2003. Inversion of high frequency surface waves with fundamental and higher modes, *J. appl. Geophys.,* **52,** 45–57.

APPENDIX A: EXPRESSIONS FOR SURFACE WAVE GREEN'S TENSOR

Here, we list a few expressions that are used in Sections 2 and 3. The analytical expression of the far-field point-force Green's tensor reads

$$\hat{G}_{nm}(\mathbf{x},\mathbf{x}_S) = \sum_{\nu} p_n^{\nu}(z,\varphi_S)\, p_m^{\nu *}(z_S,\varphi_S)\, \frac{\mathrm{e}^{-\mathrm{i}\left(k_\nu \xi_S + \frac{\pi}{4}\right)}}{\chi_\nu \sqrt{\frac{\pi}{2} k_\nu \xi_S}}. \tag{A1}$$

Here, $\mathbf{x}_S$ and $\mathbf{x}$ denote source and receiver coordinates, respectively, z_S and z are the associated depth coordinates and φ_S is the angle in the horizontal plane indicating the direction from $\mathbf{x}_S$ to $\mathbf{x}$ (Fig. 1); ξ_S denotes the horizontal distance from $\mathbf{x}_S$ to $\mathbf{x}$. Furthermore, $p_n^{\nu}(z,\varphi_S)$ is the nth component of a polarization vector associated with mode ν at the receiver [$p_m^{\nu}(z_S,\varphi_S)$ is similarly related to the source]:

$$\mathbf{p}^{\nu}(z,\varphi_S) = \begin{bmatrix} r_1^{\nu}(z)\cos(\varphi_S) \\ r_1^{\nu}(z)\sin(\varphi_S) \\ -\mathrm{i} r_2^{\nu}(z) \end{bmatrix}, \tag{A2}$$

where r_1^{ν} and r_2^{ν} are the modal eigenfunctions associated with radial and vertical displacements, respectively. In general, the eigenfunctions can only be calculated numerically; we used an algorithm based on Hisada (1994) and Lai & Rix (1998). Finally, k_ν is the modal wavenumber, and

$$\chi_\nu = 8 c_\nu U_\nu I_1^{\nu}, \tag{A3}$$

where c_ν and U_ν denote the modal phase and group velocities, respectively, which are obtained numerically, using the same algorithm. The modal kinetic energy is given as (Aki & Richards 2002)

$$I_1^{\nu} = \frac{1}{2}\int_0^{\infty} \rho(z)\left[(r_1^{\nu})^2 + (r_2^{\nu})^2\right] \mathrm{d}z, \tag{A4}$$

where $\rho(z)$ denotes the mass density.

In Section 2, spatial derivatives ∂_k are applied to the point-force response (*cf.* eqs 2 and 7). Taking only the far-field terms, we get

$$n_j c_{njkl}(\mathbf{x})\partial_k \hat{G}_{lm}(\mathbf{x},\mathbf{x}_S) = \sum_{\nu} T_n^{\nu}(z,\varphi_S)\, p_m^{\nu *}(z_S,\varphi_S) \times \frac{\mathrm{e}^{-\mathrm{i}\left(k_\nu \xi_S + \frac{\pi}{4}\right)}}{\chi_\nu \sqrt{\frac{\pi}{2} k_\nu \xi_S}}, \tag{A5}$$

$$n_j c_{njkl}(\mathbf{x})\partial_k \hat{G}_{il}(\mathbf{x}_R,\mathbf{x}) = \sum_{\nu} p_i^{\nu}(z_R,\varphi_R)\, T_n^{\nu *}(z,\varphi_R) \times \frac{\mathrm{e}^{-\mathrm{i}\left(k_\nu \xi_R + \frac{\pi}{4}\right)}}{\chi_\nu \sqrt{\frac{\pi}{2} k_\nu \xi_R}}, \tag{A6}$$

where ∂_k thus has been applied at $\mathbf{x}$. The obtained vector $T_n^{\nu} = \tau_{nj}^{\nu} n_j$, where τ_{nj}^{ν} is related to the modal stress tensor; τ_{nj}^{ν} is not the full stress tensor, but only contains its z dependence. Therefore, T_n^{ν} can be referred to as a traction vector associated with mode ν (Halliday & Curtis 2008), but actually the vector only captures the z dependence of the traction. Using $c_{njkl} = \lambda\delta_{nj}\delta_{kl} + \mu(\delta_{nk}\delta_{jl} + \delta_{nl}\delta_{jk})$ for the isotropic layers [λ and μ are the piecewise constant (in z-direction) Lamé parameters], the stress components can be expressed in terms of the eigenfunctions and read (Aki & Richards 2002; Halliday & Curtis 2008)

$$\begin{aligned}
\tau_{xx}^{\nu} &= -\mathrm{i}k_\nu\left[\lambda r_1^{\nu} + \frac{\lambda}{k_\nu}\partial_z r_2^{\nu} + 2\mu r_1^{\nu}\cos^2(\varphi_S)\right], \\
\tau_{xy}^{\nu} &= -\mathrm{i}k_\nu\left[2\mu r_1^{\nu}\cos(\varphi_S)\sin(\varphi_S)\right], \\
\tau_{xz}^{\nu} &= k_\nu\left[-\mu r_2^{\nu}\cos(\varphi_S) + \frac{\mu}{k_\nu}\partial_z r_1^{\nu}\cos(\varphi_S)\right], \\
\tau_{yy}^{\nu} &= -\mathrm{i}k_\nu\left[\lambda r_1^{\nu} + \frac{\lambda}{k_\nu}\partial_z r_2^{\nu} + 2\mu r_1^{\nu}\sin^2(\varphi_S)\right], \\
\tau_{yz}^{\nu} &= k_\nu\left[-\mu r_2^{\nu}\sin(\varphi_S) + \frac{\mu}{k_\nu}\partial_z r_1^{\nu}\sin(\varphi_S)\right], \\
\tau_{zz}^{\nu} &= -\mathrm{i}k_\nu\left(\lambda r_1^{\nu} + \frac{\lambda}{k_\nu}\partial_z r_2^{\nu} + 2\frac{\mu}{k_\nu}\partial_z r_2^{\nu}\right),
\end{aligned} \tag{A7}$$

with, obviously, $\tau_{xy}^{\nu} = \tau_{yx}^{\nu}$, $\tau_{xz}^{\nu} = \tau_{zx}^{\nu}$ and $\tau_{yz}^{\nu} = \tau_{zy}^{\nu}$. Note the corrected typos with respect to the corresponding equations of Halliday & Curtis (2008) and the change in Fourier convention.

APPENDIX B: POINT-SPREAD FUNCTION ASSOCIATED WITH HOMOGENEOUS HALF-SPACE

In this appendix, we derive the point-spread functions associated with the Rayleigh wave in a homogeneous half-space for ideal source distribution. We show that the point-spread functions are necessarily broad in space, as opposed to the point-spread function of a body wave (Wapenaar *et al.* 2011b).

To this end, we use an analytical expression for the far-field Rayleigh wave response in 2-D that reads ($\omega \geq 0$)

$$\begin{aligned}
\hat{G}_{nm}(\mathbf{x}_R,\mathbf{x}_S) = \frac{1}{\beta}\mathrm{e}^{-\mathrm{i}\omega s_R(x_R - x_S)} \\
\times \left[\left(a_{nm}\mathrm{e}^{-\omega\gamma_P z_S} + b_{nm}\mathrm{e}^{-\omega\gamma_S z_S}\right)\mathrm{e}^{-\omega\gamma_P z_R}\right. \\
\left. + \left(c_{nm}\mathrm{e}^{-\omega\gamma_P z_S} + d_{nm}\mathrm{e}^{-\omega\gamma_S z_S}\right)\mathrm{e}^{-\omega\gamma_S z_R}\right],
\end{aligned} \tag{B1}$$

where $\beta = \partial_p \Delta|_{p=s_R}$ and $\gamma_{P,S} = (s_R^2 - s_{P,S}^2)^{1/2} > 0$, with $s_{P,S,R}$ being the wave slownesses of the compressional, shear and Rayleigh waves, respectively. The coefficients a_{nm}, b_{nm}, c_{nm} and d_{nm} are frequency-independent and known in closed form (*cf.* Drijkoningen *et al.* 2006). The Rayleigh wave denominator is denoted as $\Delta(p) = (s_S^2 - 2p^2)^2 - 4p^2\sqrt{p^2 - s_P^2}\sqrt{p^2 - s_S^2}$ (Achenbach 1973). For a homogeneous half-space, the 2-D version of the response given in eq. (3), which is generally computed numerically

(Hisada 1994; Lai & Rix 1998), is equivalent to the analytical expression in eq. (B1). We emphasize that the Rayleigh wave response only describes horizontal propagation; it assumes that the Rayleigh wave is instantaneously excited when the source is fired and that the depth profile is fully developed. It thus ignores vertical wave propagation, which is only reasonable in the far field.

We consider the situation of N sources (labelled by superscript j), which all have the same spectrum, being regularly distributed along a vertical line to the left of V (*cf.* Fig. 2). In that case, the point-spread functions can be written as (eq. 33)

$$\hat{\Gamma}_{nk}\ (z, z') = \frac{\hat{P}}{|\beta|^2} \sum_{j=1}^{N} \hat{\zeta}_{nk}^{(j)}(z, z'), \tag{B2}$$

where $\hat{P}$ is the source power spectrum, and

$$\hat{\zeta}_{nk}^{(j)} = A_{nk}^{(j)} \mathrm{e}^{-\omega\eta_{PP}} + B_{nk}^{(j)} \mathrm{e}^{-\omega\eta_{SS}} + C_{nk}^{(j)} \mathrm{e}^{-\omega\eta_{PS}} + D_{nk}^{(j)} \mathrm{e}^{-\omega\eta_{SP}}. \tag{B3}$$

Here, $\eta_{PP} = \gamma_P(z + z')$, $\eta_{SS} = \gamma_S(z + z')$, $\eta_{PS} = \gamma_P z + \gamma_S z'$, $\eta_{SP} = \gamma_S z + \gamma_P z'$, and the coefficients read

$$A_{nk}^{(j)} = a_{nm} a_{km}^* \mathrm{e}^{-2\omega\gamma_P z_S^{(j)}} + b_{nm} b_{km}^* \mathrm{e}^{-2\omega\gamma_S z_S^{(j)}} + \left(a_{nm} b_{km}^* + b_{nm} a_{km}^*\right) \mathrm{e}^{-\omega(\gamma_P+\gamma_S) z_S^{(j)}}, \tag{B4}$$

$$B_{nk}^{(j)} = c_{nm} c_{km}^* \mathrm{e}^{-2\omega\gamma_P z_S^{(j)}} + d_{nm} d_{km}^* \mathrm{e}^{-2\omega\gamma_S z_S^{(j)}} + \left(c_{nm} d_{km}^* + d_{nm} c_{km}^*\right) \mathrm{e}^{-\omega(\gamma_P+\gamma_S) z_S^{(j)}}, \tag{B5}$$

$$C_{nk}^{(j)} = a_{nm} c_{km}^* \mathrm{e}^{-2\omega\gamma_P z_S^{(j)}} + b_{nm} d_{km}^* \mathrm{e}^{-2\omega\gamma_S z_S^{(j)}} + \left(a_{nm} d_{km}^* + b_{nm} c_{km}^*\right) \mathrm{e}^{-\omega(\gamma_P+\gamma_S) z_S^{(j)}}, \tag{B6}$$

$$D_{nk}^{(j)} = c_{nm} a_{km}^* \mathrm{e}^{-2\omega\gamma_P z_S^{(j)}} + d_{nm} a_{km}^* \mathrm{e}^{-2\omega\gamma_S z_S^{(j)}} + \left(c_{nm} b_{km}^* + d_{nm} a_{km}^*\right) \mathrm{e}^{-\omega(\gamma_P+\gamma_S) z_S^{(j)}}. \tag{B7}$$

In the space–time domain, the point-spread functions read

$$\Gamma_{nk}\ (z, z', t) = \frac{P(t)}{|\beta|^2} * \sum_{j=1}^{N} \zeta_{nk}^{(j)}(z, z', t), \tag{B8}$$

where the asterisk denotes convolution over time, and every individual term of $\zeta_{nk}^{(j)}(z, z', t)$ has been transformed to the time domain. For example ($\mathcal{F}^{-1}$ denotes inverse Fourier transform; *cf.* eq. 1)

$$\mathcal{F}^{-1}\left\{a_{nm} a_{km}^* \mathrm{e}^{-\omega\left[\eta_{PP}+2\gamma_P z_S^{(j)}\right]}\right\} = 2\frac{\mathrm{Re}(a_{nm} a_{km}^*)\gamma_P \left[z + z' + 2z_S^{(j)}\right] - \mathrm{Im}(a_{nm} a_{km}^*) t}{\gamma_P^2 \left[z + z' + 2z_S^{(j)}\right]^2 + t^2}, \tag{B9}$$

where η_{PP} has been substituted, and t can be positive and negative.

Now, we choose the virtual source at the free surface ($z' = 0$) and consider the source profile (z dependence) at $t = 0$. It turns out that a specific point-spread function (eq. B8) consists of a summation of spatial pulses (similar to eq. B9; 12 for each source position) that decay in vertical direction; for increasing source depth $z_S^{(j)}$, the weight of the associated pulses decreases. The total point-spread function is therefore some broad smooth function in depth direction, even in the ideal case that many sources ($N \to \infty$) with small spacing are available. The function tends to zero when $z \to \infty$.

In ideal situation, the point-spread function does have some smearing in time as well. However, that is consistent with the point-spread function of a body wave, which is also not an exact Dirac function (Wapenaar *et al.* 2011b).